THESIS

# CHARACTERIZATION OF X-RAY TRANSMISSION AND SCATTERING DURING EQUINE RADIOLOGY PROCEDURES AT THE JOHNSON FAMILY EQUINE HOSPITAL

Submitted by

Bal K. Parajuli

Department of Environmental and Radiological Health Sciences

In partial fulfillment of the requirements

For the Degree of Master of Science

Colorado State University

Fort Collins, Colorado

Fall 2023

Master's Committee:

Advisor: Alexander Brandl

Thomas Johnson
James Lindsay

ABSTRACT

CHARACTERIZATION OF X-RAY TRANSMISSION AND SCATTERING DURING EQUINE RADIOLOGY PROCEDURES AT THE JOHNSON FAMILY EQUINE HOSPITAL

Personnel handling radioactive materials or radiation-emitting devices are at risk of exposure to ionizing radiation, directly from primary beams and indirectly from scattered beams. Hence, radiation workers are enrolled in a radiation dosimetry program to comply with regulations and effectively track exposures. Because X-ray radiation is used daily for diagnostics and therapeutics of animals at the Veterinary Teaching Hospital (VTH) of the Colorado State University (CSU), the Radiation Control Office (RCO) at CSU monitors the workers' radiation dose monthly to ensure safety and compliance. The RCO has set an ALARA Level 1 investigation at 150 millirems (mrem) in a month to keep doses As Low As Reasonably Achievable (ALARA). Personnel exceeding 150 mrem in a month are notified, and the dose is investigated. An investigation level of 150 mrem provides an opportunity for the RCO to intervene early and is low compared to the regulatory annual dose limit of 5000 mrem *per* year. Over the course of the last few years, the ALARA Level 1 has been exceeded on various occasions by radiology technicians at the Johnson Family Equine Hospital (JFEH), which is affiliated with the VTH at CSU. This project was designed to bridge a substantial knowledge gap regarding the procedures conducted at the JFEH, associated radiation doses, and the facility's suitability for large-animal veterinary applications. This experiment design characterizes the facility and anticipates radiation exposures across various

spatial points within the radiology areas, facilitating the identification of radiation exposure hotspots.

This study started with staff interview, comprehensive analysis of the daily diagnostic imaging procedures at the JFEH and cross-referencing months with elevated exposure to images. Radiation exposures in the primary beam were modelled for all Technique Factors (TFs) at various distances using SpekCalc® software generated photon fluence energy spectra. The output spectrum data were entered into an MCNP® model for dose assessment using effective dose conversion coefficients. The benchmarked outcome for Cesium-137 differed 3% from the theoretical value. An MCNP® model was used to replicate the direct measurements conducted at 1 meter. The results were consistent with exposure measured by a Biomedical Fluke 451P ionization chamber, previously published exposure measurement for the given kVp and mAs, the calculated exposure for X-ray using kVp and mAs, and the typical effective radiation dose from diagnostic X-ray published by NCRP 160.

Finally, another simulation was conducted to recreate the conditions within the radiology facility using phantoms. This simulation facilitated the quantification of effective doses across various spatial points. The simulated absorbed dose was highest in the primary beam, , and lowest at a 90-degree angle from the direction of the beam, at the same distance from the source. The absorbed dose also differed considerably in front of and behind the phantom due to photoelectric absorption.

After analyzing data, to measure dose accurately, two dosimeters are recommended, one inside and one outside the lead vest. Absorbed dose can be minimized by avoiding primary beam exposure while operating the handheld X-ray switch.

# ACKNOWLEDGEMENTS

I want to express my sincere gratitude to my advisor, Dr. Alexander Brandl, for his unwavering support and guidance throughout my studies, beginning with ERHS 530 and culminating in my thesis. His mentorship and invaluable knowledge were essential to my success. I am also profoundly grateful to Dr. Johnson, Dr. Sudowe, and Dr. Leary for their insightful feedback and unwavering support. I would like to thank Dr. Lindsay for assisting with my committee.

I am also indebted to my lab group, Justin, Dave, Sara, Paige, Joe, and Noah for their guidance, mentorship, and support. Their help was crucial in assisting me with the research process, data collection, and analysis. I would also like to thank radiology technician Sandy for her technical assistance during the measurements at the Veterinary Hospital.

I am incredibly grateful to my partner, Lina, for her unwavering support throughout this journey. I also want to dedicate this thesis to my late grandmother, who passed away this summer.

I could not have completed this thesis without the help and guidance of these amazing people. Thank you!

Disclaimer: The views expressed in this thesis are those of the author and do not reflect the official policy or position of the United State Air Force, Department of Defense, or the U.S. Government.

TABLE OF CONTENTS

# INTRODUCTION

## X-rays

X-rays are high-energy, ionizing electromagnetic radiation with wavelengths shorter than ultraviolet rays [**Table 1**]. Wilhelm Roentgen, a German physicist, discovered X-rays in 1895. Since then, X-rays have been used extensively in medicine, industry, and research. X-rays are a form of electromagnetic radiation that can penetrate objects and produce detailed images of their interior components. This makes them ideal for medical imaging, such as dental X-rays and chest X-rays. X-rays are also used in industry for quality control and inspection, and in research for studying the structure of materials.

Table 1: Electromagnetic Spectrum

| Name | Radiowaves | Microwaves | Infrared | Visible | Ultraviolet | X-rays & Gamma rays |
|---|---|---|---|---|---|---|
| **Wavelength (cm)** | $10^{12}$ - $10^{8}$ | $10^{0}$ - $10^{2}$ | $10^{-4}$ - $10^{0}$ | $10^{-4}$ | $10^{-4}$ - $10^{-8}$ | $10^{-8}$ & *lower* |

X-rays can be generated by an array of different devices such as X-ray tubes, cathode-ray tubes, linear accelerators, and multiple other sources (Johnson, 2017). X-rays are produced by accelerating an electron across a potential difference (typically kilovolts order) so that the electron is abruptly stopped (or forced to change the direction) in a target, and a portion of the kinetic energy is transformed into electromagnetic radiation, released as X-rays. Radiation produced by rapidly stopping or slowing down high energy electrons is known as *bremsstrahlung* radiation, which means "braking radiation" in German (Turner, 2010). The X-ray photons produced by this

process have a continuous energy distribution, with the maximum energy equal to the kinetic energy of the stopped electrons. X-rays with discrete energy peaks are called Characteristic X-rays. Characteristic X-rays are produced when a fast-moving electron or a photon collides with a K-shell or L-shell electron of a high-atomic number material resulting in the ejection of the electron from the shell, leaving behind an incomplete inner shell. An electron from an outer shell subsequently transitions to fill the inner shell and emits a photon in the process. The energy of the characteristic X-ray is equivalent to the energy difference between the inner and outer atomic electron shells (Turner, 2010).

**The Components of an X-ray Emitting Device**

An X-ray machines produces X-rays to image objects. A typical X-ray imaging unit consists of the following components: 1) a control panel for input; 2) an X-ray tube for the generation of the radiation; 3) an attenuator or filter to remove undesired X-rays; 4) an image receiver to visualize and interpret the results [**Fig. 1**].

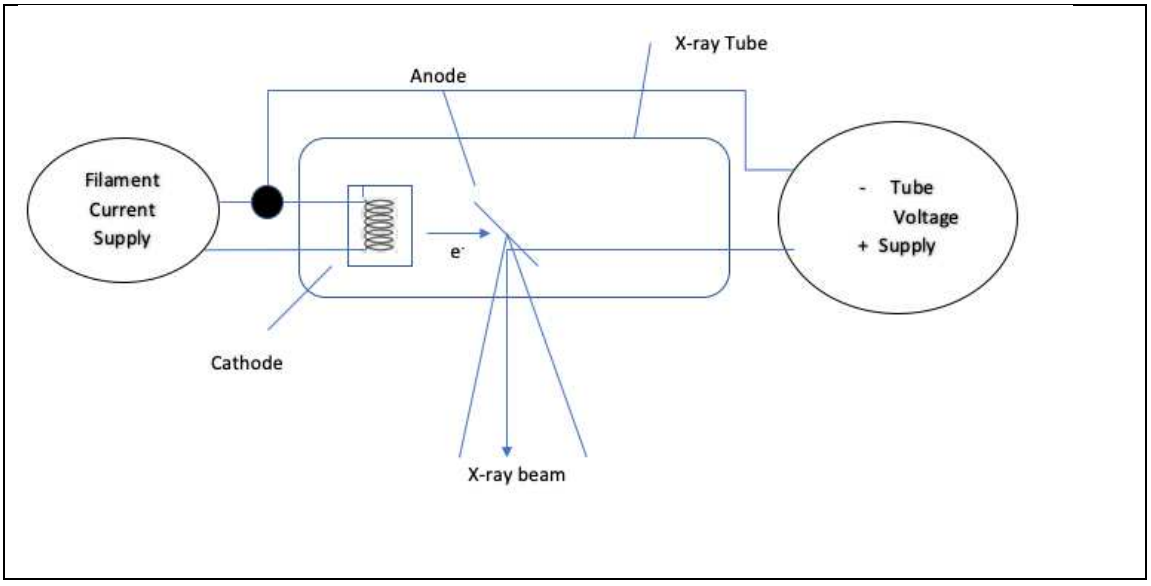


Figure 1: Schematics of X-ray production

1)The X-ray tube [Fig. 1] consists of two main components: a cathode, which emits electrons, and an anode, which is the target where the electrons collide and produce X-rays. The anode is typically made of a heavy metal with a high melting point, such as tungsten or molybdenum. It is cooled to prevent overheating and melting from the high-energy electron beam. The anode is also angled to optimize the production of X-rays and minimize heat generation.

2) The filter [Fig. 1] is a material or device that absorbs low-energy X-rays, which do not contribute to the image. Filters are used to control radiation exposure while producing high-quality images. They can be made from a variety of materials, including lead, aluminum, and copper, and can take different forms, such as sheets, blocks, or liquids.

3) The control panel [Fig. 1] is an electronic device that controls and regulates the X-ray output. It is typically located in a separate room from the X-ray tube to minimize the X-ray exposure to the operator. The control panel allows the operator to select the desired X-ray parameters, such as the voltage, current, and exposure time. It also includes safety features, such as a timer and a beam-stop switch, to prevent accidental exposure to X-rays.

4) The image receptor [Fig. 1] is a device that captures the X-rays that pass through an object and converts them into an image that can be viewed and interpreted. Image receivers can be film-based or digital.

## Diagnostic X-ray Imaging Procedures

Diagnostic X-ray imaging employs X-ray beams to create medical images of the internal anatomy of both animals and humans. These X-ray beams are generated by an X-ray tube and refined through filtration and collimation. When an X-ray beam passes through the body, it interacts with the tissues in a manner that is dependent on the tissue's density. Denser tissues, such as bone, absorb more X-rays than softer tissues, such as muscle or fat (Johnson, 2017). This difference in absorption is what allows X-rays to be used to create images of the body's internal structures.

The image receptor, which is either a wireless digital image detector or a traditional film, absorbs a portion of the X-rays' energy during this interaction. The digital detector utilizes advanced computational algorithms to process the received X-ray data and convert them into a digital image. Finally, a radiologist then interprets the image to identify any abnormalities or injuries.

## Parameters Associated with X-ray Generation

A control panel **[Fig. 1**] provides input to diagnostic X-ray tubes with specific technique factors (TFs). TFs are the settings for an X-ray machine that produce the best image for a specific anatomical region. TFs provide the operator with the proper voltage (kVp) and current and time setting (mAs) to achieve optimal images of the patient’s anatomy. The three primary parameters for X-ray generation are the electron current in milliamperes (mA), the tube potential in kilovolt peak (kVp), and the exposure time in seconds (s). Depending on the type of control panel, milliamperes and exposure time may be selected separately (mA and s) or combined as one factor, milliamperes-second (mAs) (Turner, 2010).

The mA settings on the panel controls the number of electrons flowing through the X-ray tube. The higher the mA setting, the more electrons flow through the tube and the greater the

number of X-rays produced. The exposure time setting controls the length of time that the X-ray beam is turned on. The combination of mA, kVp, and exposure time determines the quantity and quality of the X-rays produced. The kVp setting controls the voltage difference between the cathode and anode of the X-ray tube. The kVp setting is significant for determining the penetrating power of the X-rays. Higher kVp settings produce X-rays with more energy, which can penetrate thicker tissues. Lower kVp settings produce X-rays with less energy, which are more easily absorbed by tissues (Hall, 2019).

**Interaction of X-ray with Matter**

A photon can interact with matter e.g., tissues, and might be absorbed and disappear or scattered, changing its direction of travel, with or without loss of energy. (Turner,2007). Three main ways of photon interactions are photoelectric effect, Compton scattering, and pair production. Some or all of the energy of the photon is transferred to an electron in each of these interactions. The energy deposited in tissue is due to the energy transferred to electrons along their paths. Electrons can also produce secondary photons, such as bremsstrahlung and characteristic X-rays, after ionization. In soft tissue, photons with energies below 30 keV are more likely to interact with electrons through the photoelectric effect, while photons with energies between 30 keV and 25 MeV have a higher probability to interact with electrons through Compton scattering (ICRP 116, 2010).

- Photoelectric effect: a photon interacts with an electron and transfers all of its energy to the electron. This causes the electron to be ejected from the atom, leaving a vacancy behind. The vacancy is filled by an electron from a higher energy level, and this process releases a photon with energy equal to the difference between the two energy levels. (Einstein, 1905)

- Compton scattering: a photon interacts with an electron and transfers some of its energy to the electron. The photon is scattered in a different direction, and the electron is ejected from the atom. The amount of energy transferred to the electron depends on the energy of the photon and the angle at which it is scattered. (Compton, 1923)
- Pair production: a photon interacts with the nucleus of an atom and creates an electron-positron pair. (Anderson, 1932)

When an X-ray beam is absorbed by tissue, photons interact with several atoms, resulting in energy losses (Hall, 2017). The net result is the production of fast electrons, which can ionize other absorber atoms, break vital chemical bonds, and initiate a chain of events that ultimately leads to biological damage. It is therefore essential to characterize, measure, and quantify the exposure to ionizing radiation to anticipate the biological effects resulting from exposure to ionizing radiation in terms of stochastic (cancer induction, genetic effects) as well as deterministic effects (tissue effects) to have sufficient mechanisms to control these effects (Mattsson, 2013). Radiological protection in the low dose range is primarily concerned with protection against radiation-induced cancer and heritable diseases (ICRP 103, 2007). As humans cannot sense ionizing radiation, instruments must be used to detect and measure it (Johnson, 2017).

**Radiation Dosimetry**

Radiation dosimetry is the branch of science that attempts to quantitatively relate specific measurements made in a radiation field to physical, chemical, and/or biological changes that the radiation would produce in a target (Turner, 2007). Globally, the International Commission on Radiological Protection (ICRP) and the International Commission on Radiation Units and Measurements (ICRU) provide guidance on radiation protection and measurement, while the same

role is performed in the United States by the National Council on Radiation Protection and Measurements (NCRP). ICRP defines protection quantities for assessing the exposure limits whereas ICRU defines the *operational quantities* intended to provide estimates for *the protection quantities*. Conversion relationships between operational and protection quantities are clearly defined by ICRU 57 **[Fig. 2].**

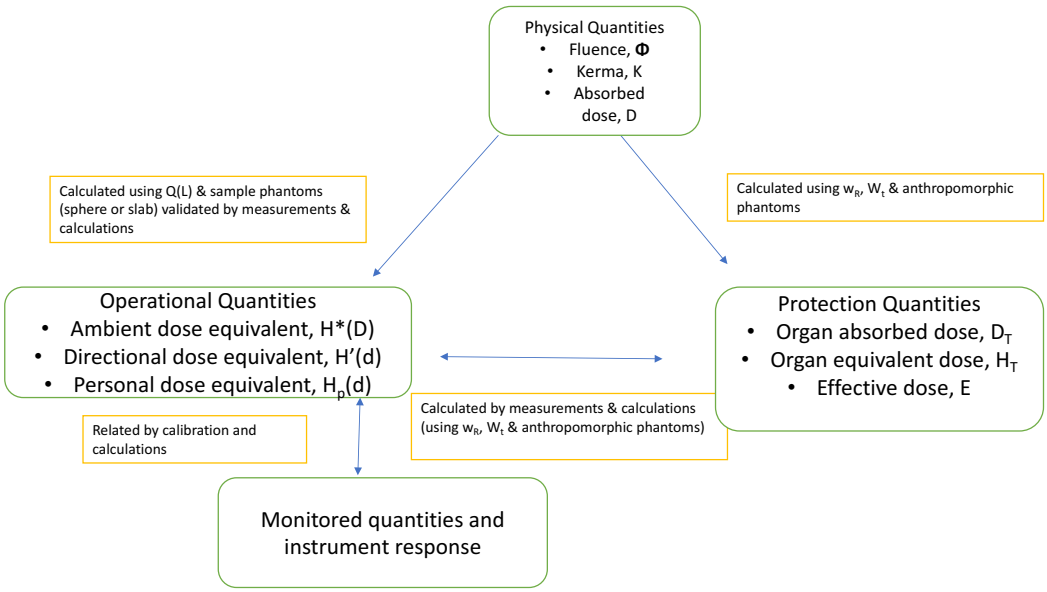


Figure 2: Relationship between physical, protection, and operational quantities

**Physical Quantities for external irradiation:**

Radiation fields external to the body can be described by *physical quantities* such as particle fluence or air kerma free in air. The quantity fluence is based on counting the number of particles incident or passing a small sphere. The fluence, $\phi$, is the quotient of *dN* by *da*, where *dN* is the number of particles incident upon a small sphere of cross-sectional area *da*, thus.

$$\phi = \frac{dN}{da} \text{ (1) (ref Mattsson, 2013)}$$

The transfer of energy from uncharged particles like photons to matter is performed by the liberation and slowing down of secondary charged particles in this matter. The kerma, *K*, is the quotient of $dE_{tr}$ by *dm*, where $dE_{tr}$ is the sum of the kinetic energies of all charged particles liberated by uncharged particles in a mass dm of material. It is given by:

$$K = \frac{dE_{tr}}{dM} \text{ (2) (ref Mattsson, 2013)}$$

The unit for kerma is Joule per kilogram (J $kg^{-1}$) or Gray (Gy).

All the dose quantities for external irradiation are based on the fundamental definition of absorbed dose in a point. The absorbed dose is the quotient of *dE* by *dM*, where *dE* is the mean energy imparted to matter in an infinitesimal volume *dV* at a point of interest in a material of density ρ during a specific period by ionizing radiation and *dM* is the mass in *dV*. The absorbed dose is defined as

$$D = \frac{dE}{dM} \text{ (3) (ref Mattsson, 2013)}$$

Fluence measures the number of particles that pass through a surface, while kerma measures the initial energy imparted by particles in a volume. Absorbed dose is a measure of the total energy deposited per unit mass. ICRP 103 defines *operational quantities* as "the quantities used in practical applications for monitoring and investigating situations involving external exposure and are defined for measurements and assessment of doses in the body." Similarly, the *protection quantities* are dose quantities that are developed for radiological protection and allow the

quantification of the extent of exposure of the human body to ionizing radiation from both whole and partial body irradiation.

**Johnson Equine Family Hospital and Radiology**

The Johnson Family Equine Hospital (JFEH) at CSU is a large, modern facility that offers comprehensive care mainly for horses and, more sporadically, for other mammals, such as donkeys and camels **[Fig.3]**. The hospital is located on the South Campus in Fort Collins, Colorado.


Figure 3: Johnson Family Equine Hospital

Large animals like horses may be taken to JFEH for surgery, treatment of complex medical conditions, or rehabilitation. For example, if a horse has a fracture, radiologists and radiological technicians at JFEH can perform X-rays to image the internal structures of the horse's leg and help

diagnose the fracture at the diagnostic imaging center for large animals. The Radiology Facility **[Fig. 4]** at the JEFH is conveniently located adjacent to the breezeway, providing easy access for patients and staff **[Fig. 1].**


Figure 4: Radiology at Johnson Family Equine Hospital

Animals are usually sedated prior to X-ray imaging to minimize animal movement during the procedure **[Fig. 5].** The process of sedating is important because movement can blur the images and make it difficult to diagnose any underlying conditions.

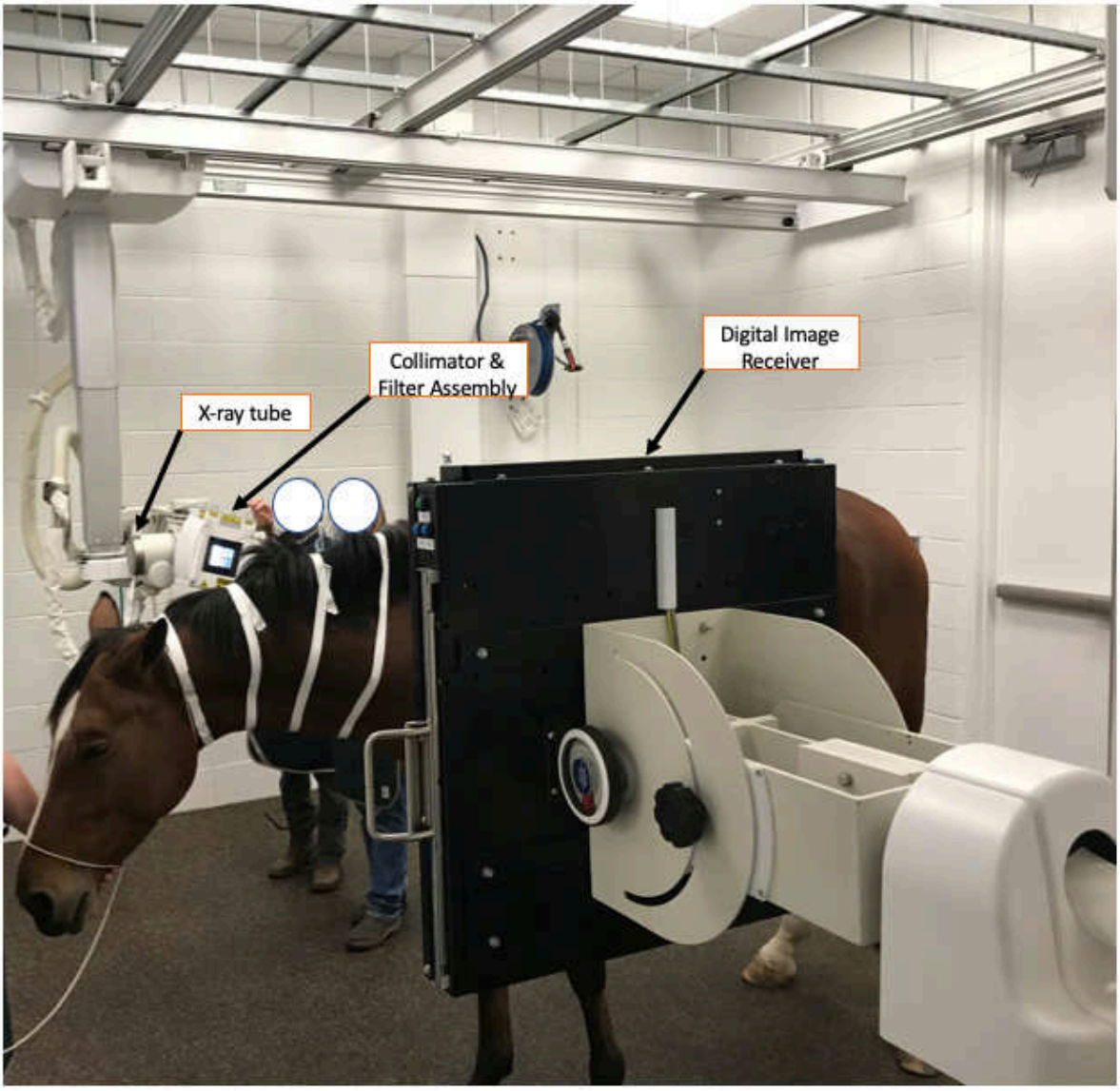


Figure 5: Equine Cervical Spine Radiograph preparation at the Johnson Family Equine Hospital

The X-ray machine used at the facility is a Vertex Rad 92 X-ray tube **[Fig. 6]** with a high-capacity CPI-Indico® 100 - 100 kW generator capable of producing 800 mA. The facility also has a Minray 80+ portable unit, an Eklin Mark III Digital System One Sound portable generator unit, and a 90+ Universal Canon Digital Radiography System with Cesium Iodide 14x17 and 11x14 wireless

active capture panels. A comprehensive overview of the equipment available in the radiology facility is provided in **Table 2.**

**Table 2:** Summary List of X-ray system

| Component | Description |
|---|---|
| Control Panel | Indico® 100 |
| X-ray Tube | Varex Imaging Rad 92 |
| Filter materials | 4.5 mm of Al equivalent |
| Image Receiver | Canon Digital Radiography System |

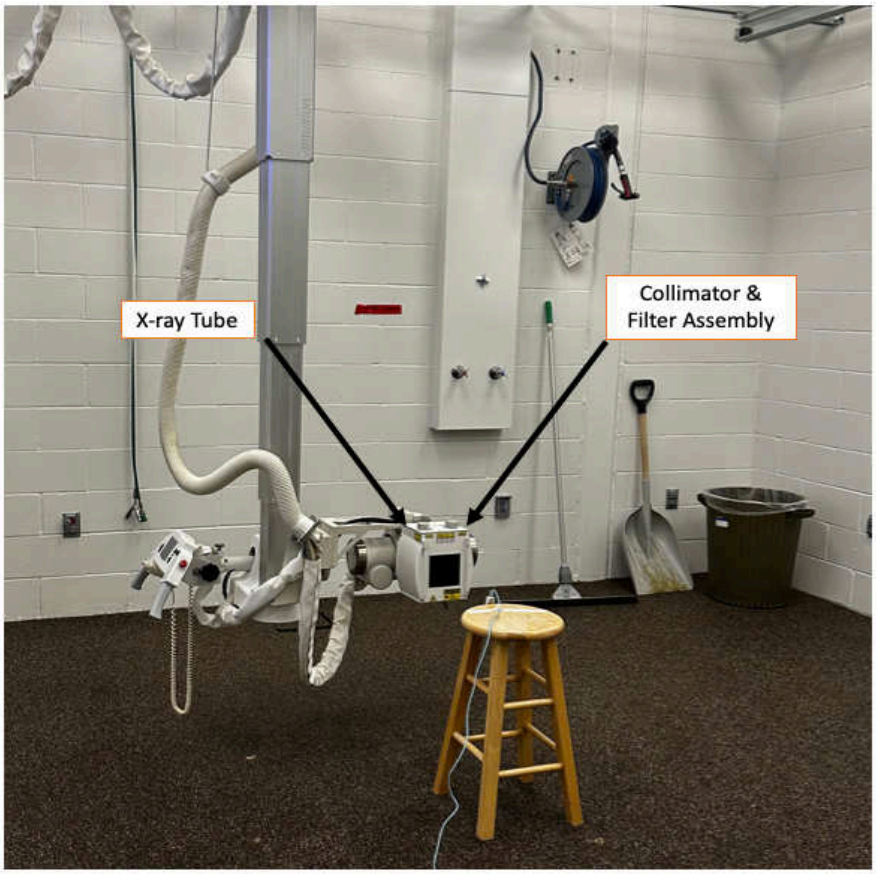


Figure 6: Diagnostic Imaging Room at Johnson Family Equine Hospital

A top view of an X-ray system showing the X-ray tube, the collimator and filter assembly inside the radiology room **[Fig. 7].**

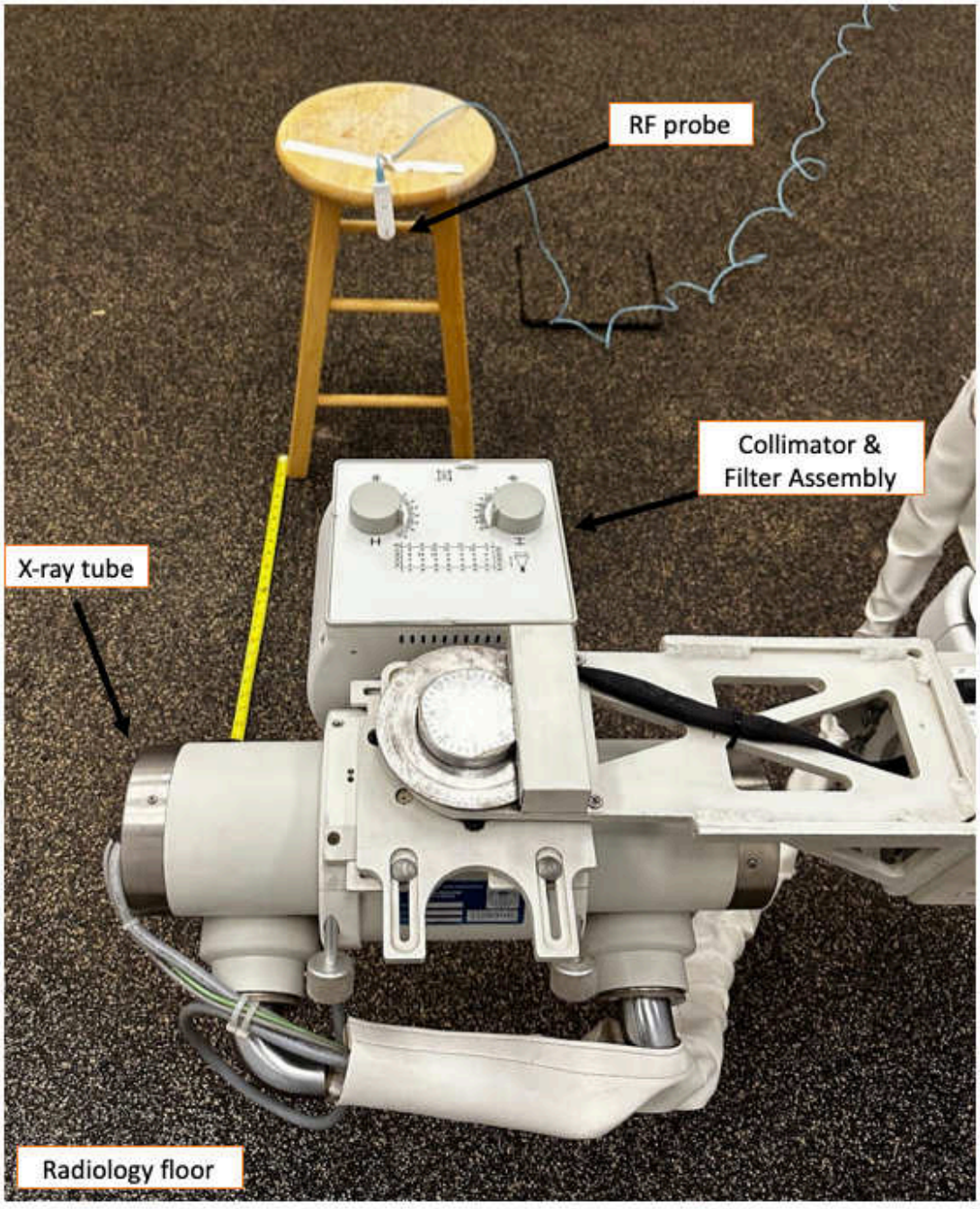


Figure 7: Top View of X-ray system at Diagnostic imaging

Here is a complete image of the instruments used at JFEH is shown in **[Fig. 8]**.

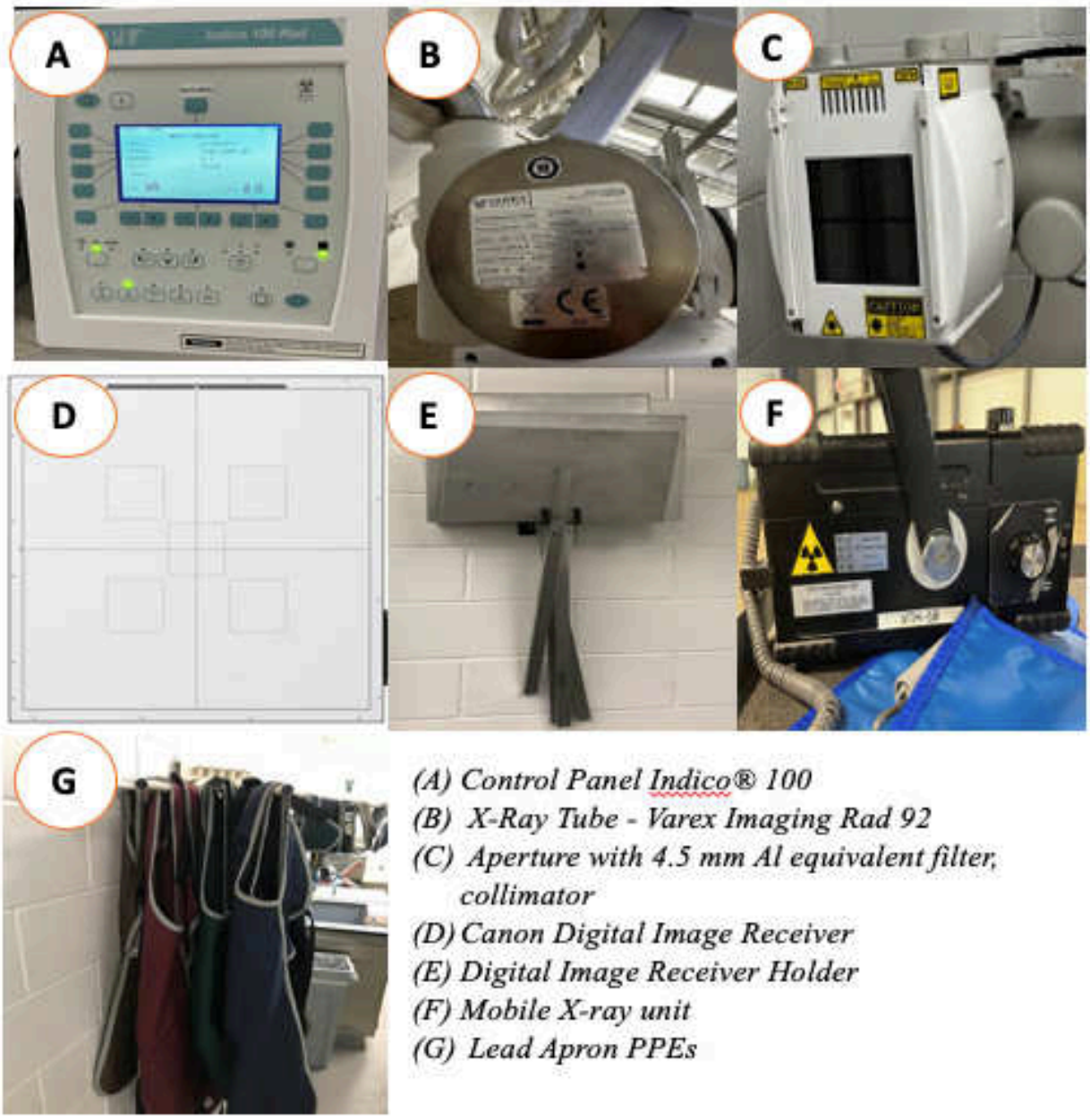


Figure 8: Equipment and PPE at Johnson Family Equine Hospital

At this facility, radiologists, radiology technicians, and veterinary school students perform examinations of the thorax, abdomen, skeleton, and other body parts. The TFs used for these images vary depending on the specific area of the body being examined, the size of the horse, and the desired level of detail. Personnel performing X-rays of various body parts utilizing TF are

summarized in **Table 3**. This table lists the type of imaging, required kilovoltage peak (kVp), current (mA), exposure time (s), or a current and exposure time combination (mAs).

Table 3: Technique Factors for Radiological Imaging at Johnson Family Equine Hospital

| Examination organ/body part | Voltage (kVp) | Current & Time combination (mAs) | Time (mS) | Examination organ/body part | Voltage (kVp) | Current & Time combination (mAs) | Time (mS) |
|---|---|---|---|---|---|---|---|
| Foot | 80 | 1.6 | - | Foot | 80 | 3.2 | - |
| Pastern/Fetlock | 80 | 1.6 | - | - | - | - | - |
| Carpus/Metacarpus/Metatarsus | 80 | 1.6 | - | - | - | - | - |
| Radius/Elbow (Lateral) | 90 | 4 | - | Radius/Elbow: CC | 90 | 6 | - |
| Shoulder | 125 | 35 | - | Shoulder: Oblique | 90 | 9 | - |
| Tarsus/Tibia (lateral/oblique) | 90 | 90 | - | Tarsus/Tibia: DP/CC | 90 | 2.4 | - |
| Stifle: Lateral/Oblique | 90 | 6 | - | Stifle CC | 96 | 10 | - |
| Hip: Lateral | 145 | 500 | 160 | Hip: VD | 145 | 500 | 200 |
| Thorax: Views 1 & 2 | 90 | 12 | - | Thorax: Views 3 | 120 | 30 | - |
| Thorax: Views 4 & 5 | 96 | 16 | - | - | 80 | 3.2 | - |
| Abdomen: View 1 & 2 | 120 | 40 | - | Abdomen: Views 3 & 4 | 100 | 25 | - |
| Sinuses/Maxilla / Mandible | 90 | 4 | - | - | - | - | - |
| Orbit/TMJ | 90 | 4 | - | - | - | - | - |
| Cervical Spine: C1-3 | 90 | 4 | - | Cervical Spine: C4-5 | 94 | 8 | - |
| Cervical Spine: C6-T1 | 100 | 20 | - | - | - | - | - |
| T/L Spine: Thoracic Dorsal Processes | 90 | 5 | - | T/L Spine: Lumbar Dorsal | 96 | 10 | - |
| T/L Spine: Thoracic Facets | 120 | 400 | 125 | T/L Spine: Lumber Facets | 145 | 500 | 200 |

High TFs are used to image T/L Thoracic Facets, T/L Spine: Lumber Facets, Hip VD, and other parts in larger animals increasing the chance for radiation exposure and scattering from X-ray photons (Lambrecht, 2017). Scattering can result in higher radiation doses to the patient and

workers. To minimize radiation dose, workers are trained in radiation safety, provided with personal protective equipment (PPE) such as lead aprons and gloves, and their exposures are tracked in a radiation dosimetry program by a Radiation Control Office (RCO).

**X-ray Beam measurement and characterizations**

Humans cannot sense ionizing radiation, so they must rely on instruments to detect and measure it. The most utilized instruments to measure radiation include *inter alia* gas-filled particle counters, scintillation counters, semiconductor detectors, personal dosimeters, and film detectors. (Johnson, 2017). To ensure the safety of individuals, accurate detection and measurement of ionizing radiation is crucial. The choice of a detector type for an X-ray application depends on the energy range of interest, the desired resolution, and the efficiency requirements (Mirion, 2023). A calculation based on the conservation of energy principle shows that an electron accelerated at a potential of 150 kVp in an X-ray tube can emit an X-ray photon with a maximum energy of 150 keV. Using the maximum potential of 150 kVp, the maximum energy of an X-ray photon ($E$) is given by, $E = h \times f = q \times V$ where $h$ is Plank's constant, $f$ is the frequency of X-ray, $q$ is the charge of the electron, and $V$ is the accelerating voltage (OpenStax, 2016).

$E = q \times V = (1.60 \times 10^{-19}\ \text{C})\ (150.0 \times 10^{3}\ \text{V})$

where, $1\ \text{C} \cdot \text{V} = 1\ \text{J}$. Using 1 eV = $1.60 \times 10^{-19}$ C;

$$E = (1.60 \times 10^{-19}\ \text{C})\ (150.0 \times 10^{3}\ \text{V})\ \frac{1\ \text{eV}}{1.60 \times 10^{-19}\ \text{C}} = 150.0 \times 10^{3}\text{eV} = 150\ \text{keV}$$

Besides instruments, software can also be utilized to model, simulate, characterize, and predict the dose associated with the X-ray field. For example, Monte Carlo N-Particle (MCNP®) transportation code can be utilized to compute a dose rate that is associated with a fluence or

current tally, either total or by energy group (Shultis, 2006). The current fluence can be generated by another software like SpekCalc® (Poludniowski, 2009).

**SpekCalc®, MCNP®, and supporting software**

*SpekCalc®*

The SpekCalc® software was developed at The Institute of Cancer Research in London, United Kingdom. The Graphical User Interface (GUI) for SpekCalc® was developed using REALbasic, Real software, Inc. SpekCalc® allows users to generate the X-ray spectra emitted from tungsten-anode X-ray tubes. The user enters the tube potential in kVp, the anode angle, and the amount of filtration. With this information, the software then generates a spectrum. The beam quality parameters can be edited, such as the half-value-layer (HVL) in mm of aluminum and copper, the mean beam energy, and the potential range of 40–300 kVp. Filtration can be selected in mm for seven materials: aluminum, copper, tungsten, tin, beryllium, water, and air. This software takes into account the underlying concepts of bremsstrahlung and characteristic X-ray production (Poludniowski, 2009).

*Monte Carlo simulations – MCNP®*

MC simulation is a computational method that can be used to estimate the scattering of radiation. MC involves using a computer program to simulate the interactions between radiation and matter, allowing predictions as to the amount of scattered radiation that will be produced in a given situation. MCNP® software, developed at Los Alamos National Laboratory (LANL), is a widely-used tool for simulating the behavior of particles in matter and radiation fields. MCNP® uses input files, also known as input decks, with specific layouts to create and model radiation transport

problems using MC methods. The input decks define the geometry of the problem set by using cell and surface cards, which in turn define the regions known as cells. Complex materials can be created in MCNP® by using standard libraries of material properties. Complex materials can be tailor-made for specific problems by assigning them to individual cells. The geometry of an MCNP® problem must be defined using cell and surface cards, and all generated cells must be assigned a material. The remainder of the universe needs to be defined as void. Once the geometry has been defined, source spectra can be defined and positioned as required. MCNP® allows users to create sources as point sources or volume sources and enables flexibility in modeling different types of radiation transport problems. (LANL, 2008).

The user can specify the desired tallies and their energy response dependencies in an MCNP® input deck. Several tallies can be recorded in MCNP®, each with its specific use depending on the scenario. The F4 cell tally is commonly used to report fluence through a specified cell, which is helpful in radiation protection. Users can also specify the number of histories or particles to optimize the statistics and balance the required computing time. Additionally, the user can scale the source activity since fluence is calculated per particle emitted. Dose quantities can then be calculated using fluence and the appropriate conversion coefficient. The F4 tally uses a track length estimate of cell fluence whereas the F5 tally tracks fluence at a point or a ring detector. The F5 tally can be positioned anywhere in the geometry to make a virtual detector with the exclusion radius around the ring defined by the user. F5 is useful for measuring dose rates at various cell locations without recreating the geometry (Shultis, 2006).

The output generated by SpekCalc®, in combination with Monte Carlo (MC) simulations, enhances the understanding of X-rays' interactions with matter and improves the accuracy of calculated energy spectra (Poludniowski, 2009).

*Visual Editor*

The Visual Editor is a software that allows users to create and visualize MCNP® input files. This software has a GUI that makes it easier to visualize complex geometries **[Fig. 9].** This software can help to reduce errors in MCNP® input files, saving users significant time and effort.

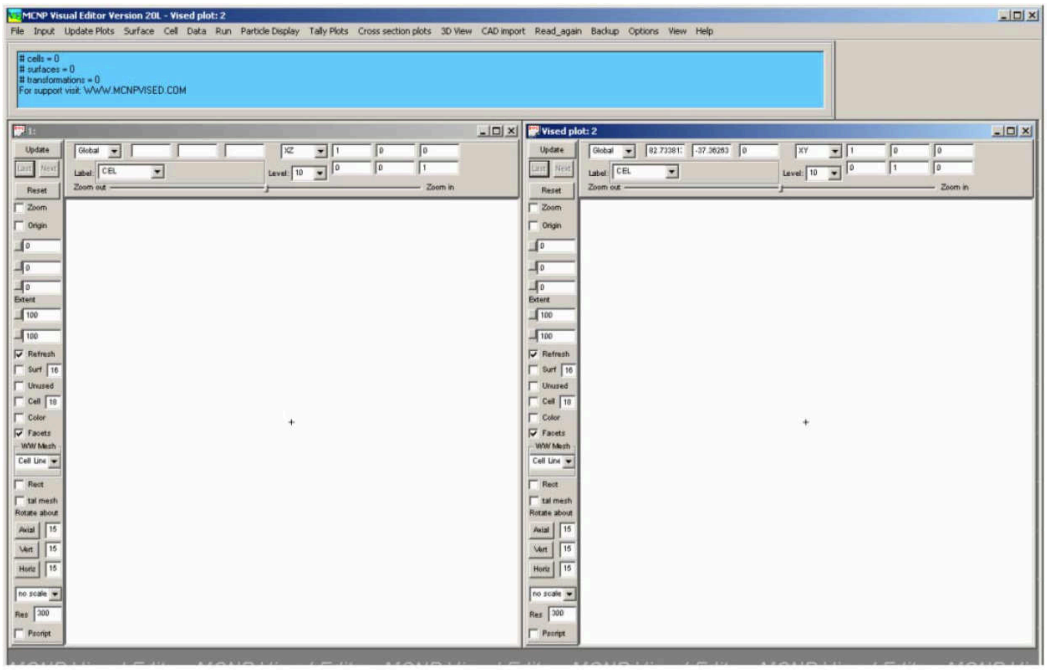


Figure 9: Startup screen of MCNP® Visual Editor

## MATERIALS & METHODS

### Experimental Design:

*Step 1* - Collection of Background Information:

a. Interview the workers at the JFEH.

b. Analyze dosimetry data and imaging rate information from the Facility to identify trends and patterns.

*Step 2* - Primary Beam Measurement:

a. Measure the air kerma in the primary beam for each TFs at 1 meter from the X-ray source, including the most common image taken at the facility.

b. Identify the imaging modality that results in the highest radiation dose. Measure the doses at 1 ft, 2 ft, 3 ft, and 1 m from the source, along with the most common image taken at the facility.

*Step 3* – Generate the X-ray Spectrum:

a. Simulate the X-ray spectra for the most common and highest dose images using the SpekCalc® software at 1 meter. Set all input parameters to resemble the X-ray tube manufacturer's specifications closely.

*Step 4* – Create Models in MCNP® and run simulations for X-ray scattering:

a. Develop a simulation code using MCNP® for the radiology room at JFEH and visualize the results with VisED®.

b. To benchmark the MCNP® code, calculate the dose from a single emission of Cs-137 and compare the simulated dose to the calculated value for each emission. This benchmarking ensures the accuracy of the code and simulated dose. Once the code is verified, it can be used to study the dose from X-ray radiation.

c. Reproduce the doses from Step 2(b) using the X-ray spectrum generated by SpekCalc® in MCNP® for benchmarking.
d. Simulate the scattered X-ray exposure at different spatial locations within the facility.

*Step 5* – Data Analysis, Result Interpretation, and Recommendations:

a. Investigate the relationship between TFs and dose using the primary beam measurement and simulation data.
b. Assess the results to determine if the elevated radiation exposure discovered by dosimetry is due to the imaging technique, other factors such as the target type, the body part's thickness, or gaps in the procedure.
c. Summarize the key findings of the study and suggest potential interventions.

**Instruments selections**

The ideal equipment needed to measure the scattered X-rays would:

1. Be lightweight.
2. Easily moved.
3. Have appropriate energy response to low energy X-rays.
4. Have appropriate response to short pulses (millisecond) of X-rays.

To measure the primary beam, a RaySafe X2 base unit **[Fig. 10]** and a Radiology/Fluoroscopy (R/F) probe were loaned from Evans Army Hospital, Fort Carson, CO, 80913. Additionally, a calibrated fluke biomedical 451P was utilized.

Figure 10: RaySafe X2 base unit and example reading

**Primary beam measurement**

The R/F probe has a high sensitivity and well-defined response to X-rays which makes the R/F probe ideal for measuring primary beam X-rays. The long cord that connects the R/F probe to the base unit allows the instrument to measure high TFs from a distance, reducing the risk of radiation exposure. The instrument details are listed in **Tables 4 and 5**.

Table 4: RaySafe X-2 base unit & Radiology/Fluoroscopy (R/F) probe utilized.

| | **X2 base unit** | **X2 R/F Sensor** |
|---|---|---|
| **Date of Use** | 13 Oct 2022 | 13 Oct 2022 |
| **Equipment:** | RaySafe X-2 base unit | RaySafe X-2 R/F Sensor |
| **Calibration Date:** | 20 July 2022 | 26 July 2022 |
| **Calibration Due** | July 2023 | July 2023 |
| **Serial number:** | 271872 | 273175 |
| **Calibrated by:** | Manufacturer | Manufacturer |

Note: This instrument was loaned by Evans Army Hospital, Fort Carson, CO, 80913.

Table 5: Additional features for R/F probe are listed below (Raysafe Manual, Fluke Biomedical)

| | | | |
|---|---|---|---|
| **Dimensions** | 14 x 22 x 79 mm | **Operating atmospheric pressure** | 70-110 kPa |
| **Mass** | 42 g | **Backscatter** | Insensitive to scattered radiation outside 70° |
| **Storage temperature** | -25 °C to + 70 °C | **Operating temperature** | 15 – 35 °C |
| **Storage humidity** | Non-condensing | | |

**Scatter Beam Measurement**

As with the primary beam, the instrument used to measure the backscattered X-rays had to be selected carefully. Per manufactures specifications in **Table 5**, the R/F probe is insensitive to scattered radiation outside of a 70° angular range. The detector's angular range of 70° limits its ability to detect scattered photons at angles greater than that, such as 90°, making it unsuitable for backscatter measurement. Similarly, other available devices like ionization counters, scintillation counters, electronic personal dosimeters (EPDs), film dosimeters, and Geiger-Müller counters were all inadequate for accurate measurements of low-energy scattered X-rays for various reason. Few of them are discussed below.

- Ionization counter: A 451P Radiation Detector produced by Fluke Biomedical was initially considered a potential measurement device but was quickly dismissed due to its known limitations in accurately measuring low-energy scattered X-rays. The ionization chamber in this detector exhibits a low relative response at lower photon energy ranges, as shown in **Figure 11.**

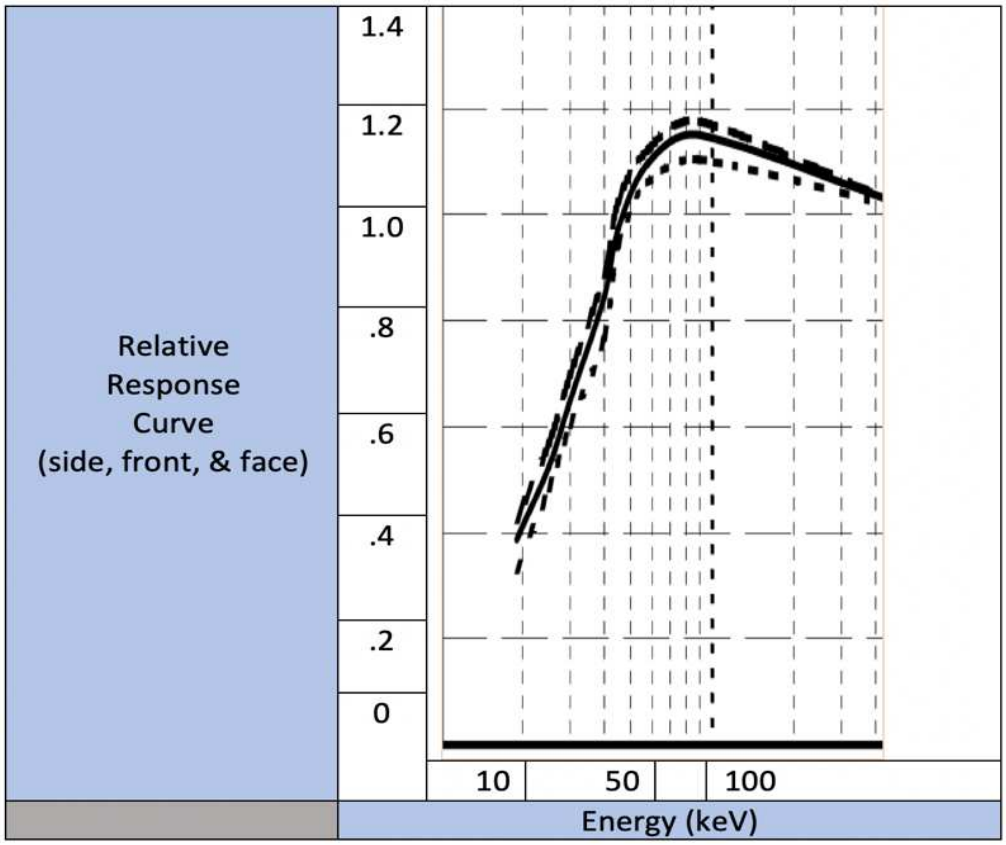


Figure 11: Energy Response of Fluke Biomedical 451P at Low Energies

- EPD: The Ludlum Model 23 Series EPDs, available at CSU laboratories could not be used as this instrument indicates estimated values for dose rate measurements in radiation fields lower than 1 mSv/h (100 mrem/h) (Ludlum, 2021).
- Scintillation detector: The use of scintillation detectors like NaI(Tl) and $LaBr_3$(Ce) detectors was deemed infeasible. These detectors require sufficient time, typically longer than a few microseconds for which the X-ray beam is turned on, to generate the energy spectrum required for analysis (Bailey, 2014).
- Film dosimeters over respond to low-energy photons below 200 keV (Turner, 2007).

Because of these reasons, a MC method was chosen. MCNP® was available for student use at CSU. The MC simulates radiation transport and allows for calculation of the radiation dose from the imaging procedures (Rogers, 2006). For the fluence input, SpekCalc was employed to generate a simulated spectrum utilizing a tungsten target with the specified settings and filters.

**Methodology**

Once the equipment and software were selected, the study began by interviewing and observing the workers. Workers were asked about their average daily workloads, work shifts, personnel, staffing, working hours, software and equipment utilized, PPE, use and storage of dosimeters, workers' knowledge of radiation safety, and other information. The Picture Archiving and Communication (PAC) system holds the details of equine X-ray images, including the TFs used. The data were analyzed to verify which X-ray images were taken during the months when the ALARA Level 1 investigation limit was exceeded by individual workers and were absent during the other months.

The RaySafe X2 with R/F probe and Fluke Biomedical 451 P were used to measure the primary beam. Beforehand, the equipment was inspected for integrity, calibration date, and operating range. Six measurements were taken at 1 meter from the surface of the X-ray unit to ensure accuracy. The measurements were taken for all TFs used in the facility. Additional measurements were taken at distances of 1 ft, 2 ft, 3 ft, and 1 m for the most frequently used image modality and the image modality with the highest TFs. Using kVp and mAs, exposures from individual TFs were calculated at 1 meter distance as well.

The following details of the X-ray equipment were noted: the manufacturer, the type of tube, the filter information, the collimator information, and the image-receiving unit information.

The details of the X-ray tube, including the type of anode, angle, thickness, and other information, were obtained from the manufacturer's website. Details obtained from the manufacturer's specifications and kVp were entered into the SpekCalc® software to generate a photon fluence, which was used in the MCNP® input deck for calculation of the absorbed dose.

An MCNP® benchmarking model was first developed. A full input deck and outputs are reported in **Appendix A**. This simulation output predicts the dose per emission from Cesium-137 using the fluence dose conversion coefficient from ICRP 116. A second input deck was then developed to specify the conditions of the radiology room. Visual Editor software was used to visualize the proper geometry of phantoms and the room. Then, the fluence data from SpekCalc® and X-ray settings were used to calculate the absorbed dose at a 1-meter distance for the highest target-to-filter (TF) setting.

Finally, a third simulation was developed to measure the absorbed doses at various locations within the room. This simulation characterized the dose and scattering for different TF settings. The doses were modeled at the following seven locations: i.) the proximal side of the horse phantom to the X-ray tube; ii.) the distal side of the horse phantom to the X-ray tube, iii) the head of the horse phantom; iv) tail of horse phantom; v) chest height of human phantom located next to horsetail; vi) the back of human phantom; vii) and directly behind the X-ray tube.

## RESULTS AND DISCUSSION

For this project I interviewed the radiology staff at the diagnostic imaging facility about their workloads, work shifts, personnel, staffing, working hours, software and equipment utilized, PPE, use and storage of dosimeters, knowledge of radiation safety, and other information. The facility is staffed by a radiology technician, one or two animal handlers, radiologists, and veterinary students. The diagnostic imaging section typically examines an average of 5 to 8 horses daily during the peak months of May to August. Three to 5 rotating veterinary students are typically present to assist with the examinations. However, there were instances when the section was short-staffed, with only one person present. The facility continued to provide radiographic imaging services despite short staffing. All the details of diagnostic images were saved into a Picture Archiving and Communication (PAC) system.

After observing the procedure over two months, this study determined that the workers avoided exposure to the primary X-ray beam. All workers had taken a radiation safety course offered by the CSU RCO. Everyone donned a lead apron and lead neck guard, safely and effectively. These personnel also put on a single OSL dosimeter outside of the PPE. Additionally, animal handlers and veterinary students not employed by the diagnostic imaging facility were present in the room while X-ray images were being taken, possibly exposing them to scattered X-ray. No written standard operating procedures (SOPs) were available in the work area.

During a comprehensive review of dosimetry data in relation to the ALARA Level 1 dose and a cross-reference of all imaging techniques using the PAC system, this study found that a radiation technician conducted four separate instances of Hip Ventrodorsal radiographs. The procedure involves positioning the X-ray tube beneath the horse and the image receptor behind the targeted hip area with an extender. Using tranquilizers on the equine subjects and positioning the

tube beneath the horse can make the horse unpredictable. To calm the horse during the procedure, a human attendant is consistently positioned at the hind limb of the horse, near the X-ray tube. This setup can potentially increase radiation exposure due to scattered X-rays, especially when high TFs are used. The possible exposure was studied in detail during this research.

Data collection for this study began by measuring Air KERMA for all TFs utilized at the Radiology facility. The measurements were taken at 1 meter from the X-ray tube, in the primary beam using a RaySafe X-2 R/F probe. To ensure accuracy, the parameters used by the diagnostic imaging technicians for specific TF settings tailored for distinct imaging procedures were adopted. Each measurement was taken 6 times to increase precision. Notably, the TF utilized for Thoracolumbar (T/L) Spine: Lumber Facets had the highest average KERMA of 62.2 mGy. The most utilized TF, Stifle Lateral/Oblique Radiography, had an average KERMA of 0.63 mGy. The measured values shown in **Table 6** were significantly higher than the anticipated dose.

Table 6: List of radiography image modality, setting used, and dose measured at 1 m distance

| | Voltage | Current & Time | Time | Dose |
|---|---|---|---|---|
| **Irradiated Body Parts** | (kVp) | (mAs) | (mS) | (mGy) |
| Foot | 80 | 1.6 | - | 0.32 |
| Foot | 80 | 3.2 | - | 0.64 |
| Pastern/Fetlock | 80 | 1.6 | - | 0.32 |
| Carpus/Metacarpus/Metatarsus | 80 | 1.6 | - | 0.32 |
| Radius/Elbow (Lateral) | 90 | 4 | - | 1 |
| Radius/Elbow: CC | 90 | 6 | - | 1.56 |
| Shoulder | 125 | 35 | - | 23.65 |
| Shoulder: Oblique | 90 | 9 | - | 2.5 |
| Tarsus/Tibia (lateral/oblique) | 90 | 2 | - | 0.51 |
| Tarsus/Tibia: DP/CC | 90 | 2.4 | - | 0.63 |
| Stifle: Lateral/Oblique | 90 | 6 | - | 1.5 |
| Stifle CC | 96 | 10 | - | 2.8 |
| Hip: Lateral * | 145 | 500 | 160 | 49.31 |
| Hip: VD * | 145 | 500 | 200 | 61.5 |
| Thorax: Views 1 & 2 | 90 | 12 | - | 13.15 |
| Thorax: Views 3 | 120 | 30 | - | 13.7 |
| Thorax: Views 4 & 5 | 96 | 16 | - | 4.58 |
| Abdomen: View 1 & 2 | 120 | 40 | - | 17.51 |
| Abdomen: Views 3 & 4 | 100 | 25 | - | 7.8 |
| Sinuses/Maxilla/ Mandible | 90 | 4 | - | 1 |
| Orbit/TMJ | 90 | 4 | - | 1 |
| Cervical Spine: C1-3 | 90 | 4 | - | 1 |
| Cervical Spine: C4-5 | 94 | 8 | - | 2.8 |
| Cervical Spine: C6-T1 | 100 | 20 | - | 10.3 |
| T/L Spine: Thoracic Dorsal | 90 | 5 | - | 1.25 |
| T/L Spine: Lumbar Dorsal | 96 | 10 | - | 2.25 |
| T/L Spine: Thoracic Facets * | 120 | 400 | 125 | 21.96 |
| T/L Spine: Lumber Facets * | 145 | 500 | 200 | 61.77 |
| T/L Spine: Lumber Facets * | 145 | 500 | 120 | 51.07 |

*Note: Some techniques utilize specific current and time rather than a combination.*

Stifle Lateral/Oblique Radiography and T/L Spine: Lumber Facets were studied further at 1 foot, 2 feet, 3 feet, and 1 meter **[Table 7]**. RaySafe R/F probe measured air KERMA, millimeters of aluminum Half Value Layer (HLV), pulse count, and the millimeters of aluminum transmission factor. By using the data collected, a dose distance curve was

generated. This curve was used to validate the efficacy of the instrument by assessing the inverse square law.

Table 7: Stifle Lateral/Oblique measurements at various distances

| **Measurement** | **Distance** | **Air Kerma** | **Pulse Duration** | **Half value layer** | **Dose rate** | **Number of pulse** | **Total filtration** |
|---|---|---|---|---|---|---|---|
| | (ft) | (µGy) | (ms) | mm Al HVL | $(\frac{\text{mGy}}{\text{s}})$ | pulse | mm Al TF |
| 1 | 1 | 303.5 | 10.3 | 3.43 | 29.61 | 1 | 3.5 |
| 2 | 1 | 305.8 | 10.3 | 3.39 | 29.84 | 1 | 3.5 |
| 3 | 1 | 306.5 | 10.3 | 3.38 | 29.9 | 1 | 3.4 |
| 4 | 1 | 306.2 | 10.2 | 3041 | 30.06 | 1 | 3.5 |
| 5 | 1 | 306.2 | 10.2 | 3.42 | 30.06 | 1 | 3.5 |
| 6 | 1 | 306.5 | 10.2 | 3.41 | 30.09 | 1 | 3.5 |
| 7 | 1 | 307.7 | 10.3 | 3.4 | 30.02 | 1 | 3.5 |
| 8 | 2 | 114.7 | 10.2 | 3.39 | 11.26 | 1 | 3.5 |
| 9 | 2 | 114 | 10.3 | 3.36 | 11.12 | 1 | 3.5 |
| 10 | 2 | 114.2 | 10.2 | 3.4 | 11.21 | 1 | 3.5 |
| 11 | 2 | 114.5 | 10.3 | 3.39 | 11.17 | 1 | 3.6 |
| 12 | 2 | 114.8 | 10.3 | 3.4 | 11.2 | 1 | 3.6 |
| 13 | 2 | 114.8 | 10.3 | 3.39 | 11.2 | 1 | 3.5 |
| 14 | 3 | 65.99 | 10.2 | 3.28 | 6.477 | 1 | 3.4 |
| 15 | 3 | 66.52 | 10.2 | 3.29 | 6.529 | 1 | 3.4 |
| 16 | 3 | 66.75 | 10.2 | 3.27 | 6.552 | 1 | 3.4 |
| 17 | 3 | 66.54 | 10.3 | 3.26 | 6.491 | 1 | 3.3 |
| 18 | 3 | 66.68 | 10.3 | 3.27 | 6.505 | 1 | 3.3 |
| 19 | 3 | 66.79 | 10.2 | 3.27 | 6.556 | 1 | 3.4 |
| 20 | 3.28 | 52.09 | 52 | 3.27 | 5.051 | 1 | 3.2 |
| 21 | 3.28 | 52.06 | 10.3 | 3.31 | 5.049 | 1 | 3.4 |
| 22 | 3.28 | 51.86 | 10.3 | 3.31 | 5.028 | 1 | 3.4 |
| 23 | 3.28 | 52.18 | 10.3 | 3.31 | 5.06 | 1 | 3.4 |
| 24 | 3.28 | 51.71 | 10.3 | 3.34 | 5.015 | 1 | 3.5 |
| 25 | 3.28 | 51.97 | 10.3 | 3.31 | 5.04 | 1 | 3.4 |

Analysis of the these data **[Table 8]** revealed that the measurement for absorbed dose at a particular distance had a high precision and low standard deviation. Table 9 shows the average absorbed dose at various distances.

Table 8: Data Analysis

| **Distance** (ft.) | **Mean** (mGy) | **Standard deviation** (mGy) |
|---|---|---|
| 1 | 30.61 | 0.13 |
| 2 | 11.45 | 0.03 |
| 3 | 6.65 | 0.03 |
| 3.28 | 5.20 | 0.02 |

Using data displayed in Table 9, a curve for dose and square of distance from the X-ray tube was created **[Fig. 12].** A regression line has a coefficient of determinant ($R^2$) of 0.81 showing square of distance and dose values fit the curve and follow the inverse square law.

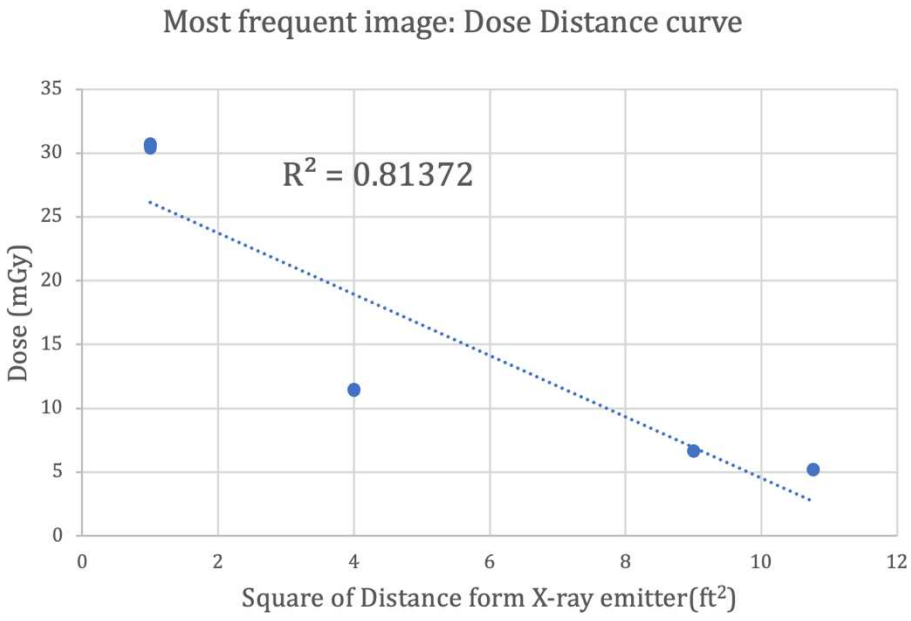


Figure 12: Stifle Lateral/Oblique Facet Dose Distance Curve

A summary for T/L Spine: Lumber Facets is shown in **Table 9**.

Table 9: T/L Spine: Lumber Facets measurements at various distances

| **Measurement** | **Distance** | **Air Kerma** | **Pulse Duration** | **Half value layer** | **Dose rate** | **Number of pulses** | **Total filtration** |
|---|---|---|---|---|---|---|---|
| | (ft) | (µGy) | (ms) | mm Al HVL | $(\frac{mGy}{s})$ | pulse | mm Al TF |
| 1 | 146.2 | 60.16 | 250.3 | 6.05 | 240.4 | 1 | - |
| 1 | 146.1 | 60.15 | 250.2 | 6.05 | 240.4 | 1 | - |
| 1 | 146 | 60.18 | 250.2 | 6.05 | 240.5 | 1 | - |
| 1 | 146.1 | 60.17 | 250.2 | 6.05 | 240.5 | 1 | - |
| 1 | 146.1 | 60.24 | 250.2 | 6.05 | 240.8 | 1 | - |
| 1 | 146.1 | 42.27 | 175.4 | 6.05 | 241 | 1 | - |
| 2 | 143.8 | 31.27 | 250.1 | 5.66 | 125 | 1 | - |
| 2 | 143.5 | 31.23 | 250.2 | 5.67 | 124.8 | 1 | - |
| 2 | 143.5 | 31.33 | 250.2 | 5.67 | 125.2 | 1 | - |
| 2 | 143.9 | 31.18 | 250.2 | 5.65 | 124.6 | 1 | - |
| 2 | 143.5 | 31.17 | 250.2 | 5.67 | 124.6 | 1 | - |
| 2 | 143.4 | 31.14 | 250.2 | 5.66 | 124.5 | 1 | - |
| 3 | 144.4 | 9.633 | 141.2 | 5.67 | 68.2 | 1 | - |
| 3 | 144.7 | 13.54 | 198.5 | 5.67 | 68.2 | 1 | - |
| 3 | 144.6 | 17.05 | 250.3 | 5.66 | 68.13 | 1 | - |
| 3 | 144.2 | 17.04 | 250.2 | 5.67 | 68.1 | 1 | - |
| 3 | 144.2 | 17.16 | 250.2 | 5.66 | 68.6 | 1 | - |
| 3 | 144.5 | 17.21 | 250.2 | 5.66 | 68.8 | 1 | - |
| 3.28 | 144.5 | 14.9 | 250.3 | 5.65 | 59.55 | 1 | - |
| 3.28 | 144.6 | 14.88 | 350.3 | 5.65 | 59.45 | 1 | - |
| 3.28 | 144.6 | 14.85 | 250.2 | 5.65 | 59.36 | 1 | - |
| 3.28 | 144.6 | 14.83 | 250.2 | 5.65 | 59.26 | 1 | - |
| 3.28 | 144.4 | 14.8 | 250.2 | 5.65 | 59.14 | 1 | - |
| 3.28 | 144.2 | 14.8 | 250.2 | 5.66 | 59.15 | 1 | - |

The measured values were significantly higher than the anticipated dose. **Table 10** shows the average dose at the various distances.

Table 10: Data Analysis

| **Distance** (ft.) | **Mean** (mGy) | **Standard deviation** (mGy) |
|---|---|---|
| 1 | 57.20 | 0.04 |
| 2 | 31.22 | 0.07 |
| 3 | 15.27 | 3.11 |
| 3.28 | 14.84 | 0.04 |

**Fig. 13** shows a goodness-of-fit plot for dose versus the square of distance from the X-ray tube. The regression line has a coefficient of determination ($R^2$) of 0.90, indicating that 90% of the variation in the measured dose can be explained by the square of the distance from the X-ray. This shows a close resemblance to the inverse square law. The standard deviation at 3 ft was higher when the X-ray tube was on for a partial duration of 141 microseconds (ms) and 198 ms, compared to the full 250 ms.

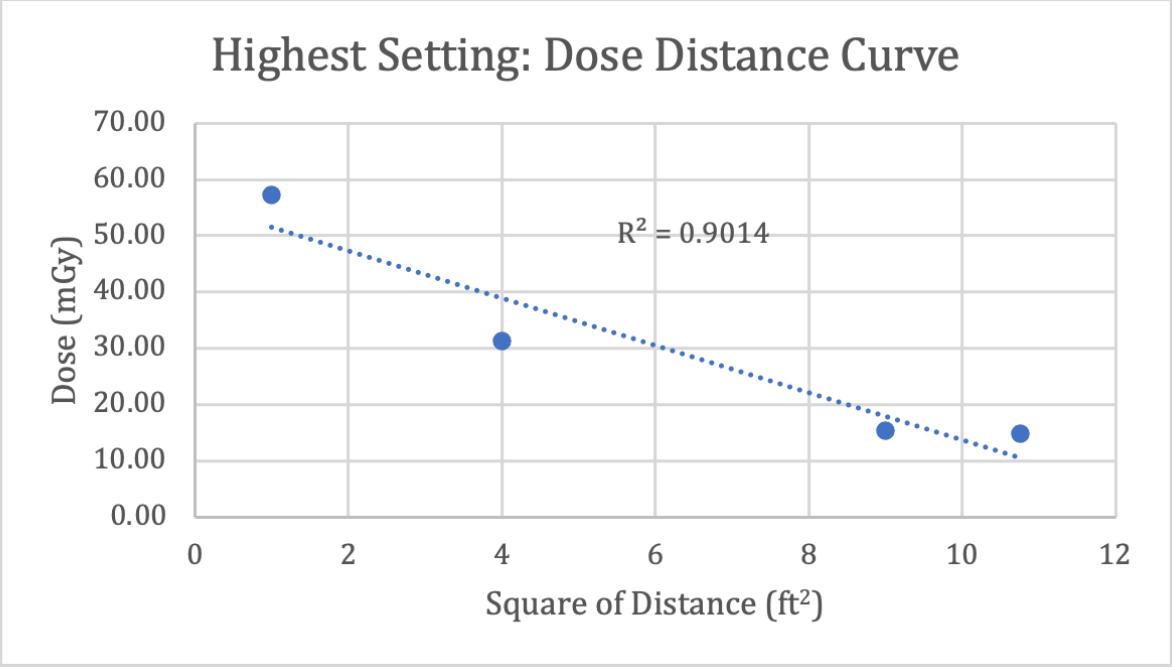


Figure 13: T/L Stifle Lumber Facets Dose distance curve

The measured values were significantly higher than the modeled dose, so a second set of measurements was taken using a 451P to validate the accuracy of the exposure from the primary beam. This second set of measurements was consistent with the previously published exposure measurement for the given kVp and mAs, the calculated exposure for X-ray using kVp and mAs, and the typical effective radiation dose from diagnostic X-ray (NCRP 160). Table 11 shows the TFs (kVp and mAs), the calculated dose from single and multiphase X-ray, the measured dose from the 451P, and the previous measurement from R/F probe, the calculated uncertainty in the exposure measurement from the relative response of 451 P meter, and comparable doses from a typical X-ray. The calculated doses were evaluated using the following equation.

$$\text{Output}\,(mR) = \text{k} \times \text{kiloVoltagepeak}^2 \times \text{current} \times \text{time} \times \frac{1}{\text{distance}^2}$$

Where k = $6.53 \times 10^{-4}$ mR / mAs; kiloVoltagepeak in V, time in s, current in mA, distance in cm were taken from Table 3, and measured at 100 cm distance. (Kothan, 2011)

**Table 11** shows all TFs in ascending order to simplify the chart. The asterisk (*) and double asterisk (**) symbols indicate the most common imaging technique and the image with the highest TF combination, respectively. The table also shows calculated values for single-phase and multiphase X-ray doses at 1 m, along with readings from a Fluke Biomedical 451P gas ionization chamber and a Biomedical RaySafe X-2 with an R/F probe for X-ray doses at 1 m. As shown in Fig. 11, 451 P ionization chamber is a relative response at various energies of photon leading to inaccuracies in measurement. The calculated uncertainty in the exposure measurement from relative response of 451 P meter is also included in the **Table 11**. X-ray dose readings at the operating energy range is also shown. The last column shows an individual's estimated dose from one X-ray with a similar TF.

Table 11: List of setting used, calculated, measured and measured at 1 m distance

| | *kVp* | *mAs* | Single Phase X-ray (*mGy*) | Multi-phase X-ray (*mGy*) | 451 P Measured (mGy) | R/F Measured (*mGy*) | | 451 P relative response error (*mGy*) | Human Equivalent |
|---|---|---|---|---|---|---|---|---|---|
| | 80 | 1.6 | 0.03 | 0.06 | 0.02 | 0.32 | ± | 0.01 | Chest –ray |
| | 80 | 3.2 | 0.06 | 0.12 | 0.08 | 0.64 | ± | 0.02 | |
| | 90 | 2 | 0.05 | 0.09 | 0.04 | 0.51 | ± | 0.01 | |
| | 90 | 2.5 | 0.06 | 0.12 | 0.04 | 0.68 | ± | 0.01 | |
| | 90 | 4 | 0.09 | 0.19 | 0.10 | 1.00 | ± | 0.03 | |
| | 90 | 5 | 0.12 | 0.23 | 0.09 | 1.25 | ± | 0.03 | |
| * | 90 | 6 | 0.14 | 0.28 | 0.14 | 1.37 | ± | 0.04 | Thoracic |
| | 90 | 6.3 | 0.15 | 0.29 | 0.12 | 1.55 | ± | 0.04 | |
| | 90 | 10 | 0.23 | 0.46 | 0.14 | 2.50 | ± | 0.04 | |
| | 90 | 12 | 0.28 | 0.56 | 0.24 | 11.53 | ± | 0.07 | |
| | 94 | 8 | 0.20 | 0.41 | 0.16 | 2.46 | ± | 0.05 | |
| | 96 | 10 | 0.26 | 0.53 | 0.21 | 1.97 | ± | 0.06 | |
| | 96 | 16 | 0.42 | 0.85 | 0.41 | 4.02 | ± | 0.12 | |
| | 100 | 20 | 0.57 | 1.15 | 0.54 | 6.84 | ± | 0.16 | |
| | 100 | 25 | 0.72 | 1.43 | 0.55 | 9.03 | ± | 0.17 | Abdomen AP |
| | 120 | 30 | 1.24 | 2.48 | 1.68 | 12.01 | ± | 0.51 | |
| | 120 | 40 | 1.65 | 3.30 | 1.25 | 15.36 | ± | 0.38 | |
| | 120 | 80 | 3.30 | 6.61 | 2.35 | 19.26 | ± | 0.70 | |
| | 125 | 32 | 1.43 | 2.87 | 1.20 | 20.74 | ± | 0.36 | |
| | 145 | 75 | 4.52 | 9.04 | 4.88 | 13.07 | ± | 1.46 | |
| ** | 145 | 100 | 6.03 | 12.06 | 4.10 | 13.07 | ± | 1.23 | CT scan |

The measured values by ionization chamber were consistently lower than calculated dose values as the X-rays system had a 3.5 mm equivalent of aluminum filter to remove lower energy X-ray photons. A dose and distance curve were created to validate the inverse square law as detailed in **Table 12**.

Table 12: Distance and dose for most common imaging technique

| Distance (cm) | 70 | 80 | 90 | 100 | 110 | 120 | 130 |
|---|---|---|---|---|---|---|---|
| Dose (mGy) | 0.274 | 0.206 | 0.159 | 0.134 | 0.128 | 0.084 | 0.076 |
| Distance ($cm^2$) | 4900 | 6400 | 8100 | 10000 | 12100 | 14400 | 16900 |

**Fig. 14** shows a goodness-of-fit plot for dose versus the square of distance from the X-ray tube. The regression line has a coefficient of determination ($R^2$) of 0.88, indicating that 88% of the variation in the measured dose can be explained by the square of the distance from the X-ray. This shows a close resemblance to inverse square law.

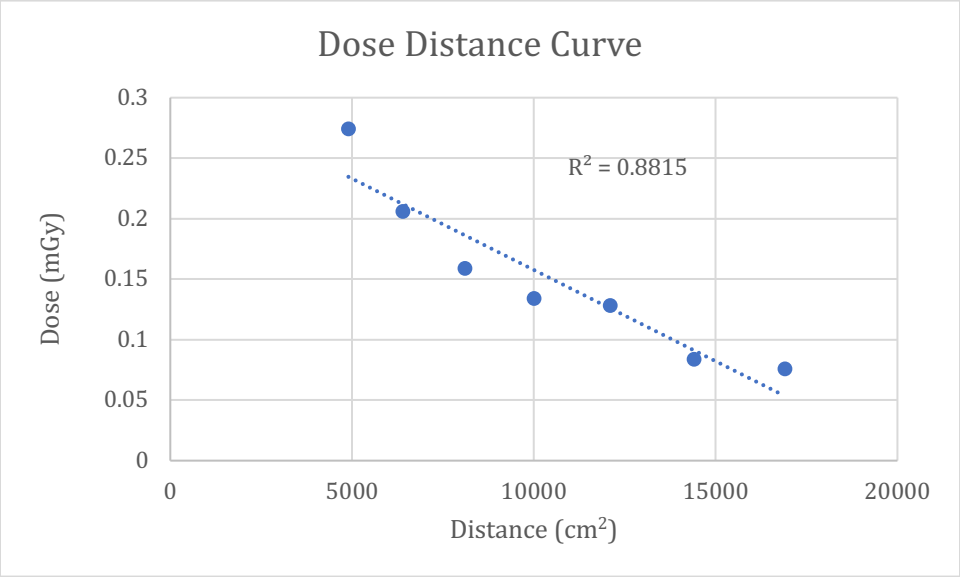

Figure 14: Dose-Distance Curve to validate inverse square law

After these initial baseline evaluations of the data, the SpekCalc® software was used to generate the photon fluence spectrum of the X-ray tube **[Table 13]**. As the facility used Varex Imaging Rad 92 model X-ray tube, all input parameters aligned closely to the manufacturer's specifications. Parameters used are as follows: a filtration material and thickness of 3.5 mm of Aluminum equivalent, a target anode material of Tungsten, and a target angle of 12 degrees. The peak voltage applied to the X-ray tube matched most common and highest setting TFs. Photon fluence as the count of photons with specific energy *per* square centimeter area *per* milliampere-second, corresponding to the highest kVp of 150 keV are summarized in **Table 14**.

Table 13: Tabulated SpekCalc Photon Fluence Spectrum

| **Energy** (MeV) | **N** $(\frac{\text{keV cm}^2}{\text{mAs}})$ | **Energy** (MeV) | **N** $(\frac{\text{keV cm}^2}{\text{mAs}})$ | **Energy** (MeV) | **N** $(\frac{\text{keV cm}^2}{\text{mAs}})$ |
|---|---|---|---|---|---|
| 0.05 | 4.38E+06 | 0.088 | 2.11E+06 | 0.126 | 765535.6 |
| 0.051 | 4.36E+06 | 0.089 | 2.07E+06 | 0.127 | 737031.9 |
| 0.052 | 4.34E+06 | 0.09 | 2.03E+06 | 0.128 | 708945.6 |
| 0.053 | 4.31E+06 | 0.091 | 1.98E+06 | 0.129 | 680839 |
| 0.054 | 4.28E+06 | 0.092 | 1.94E+06 | 0.130 | 652832.6 |
| 0.055 | 4.24E+06 | 0.093 | 1.90E+06 | 0.131 | 624517.5 |
| 0.056 | 4.19E+06 | 0.094 | 1.86E+06 | 0.132 | 597614.2 |
| 0.057 | 4.14E+06 | 0.095 | 1.82E+06 | 0.133 | 569244.2 |
| 0.058 | 1.75E+07 | 0.096 | 1.78E+06 | 0.134 | 541843.5 |
| 0.059 | 2.76E+07 | 0.097 | 1.74E+06 | 0.135 | 514620.6 |
| 0.06 | 3.98E+06 | 0.098 | 1.70E+06 | 0.136 | 486829.5 |
| 0.061 | 3.92E+06 | 0.099 | 1.66E+06 | 0.137 | 459045.9 |
| 0.062 | 3.86E+06 | 0.100 | 1.62E+06 | 0.138 | 432375.7 |
| 0.063 | 3.79E+06 | 0.101 | 1.58E+06 | 0.139 | 404000 |
| 0.064 | 3.73E+06 | 0.102 | 1.55E+06 | 0.140 | 376462 |
| 0.065 | 3.67E+06 | 0.103 | 1.51E+06 | 0.141 | 349222.8 |
| 0.066 | 3.60E+06 | 0.104 | 1.47E+06 | 0.142 | 318878.7 |
| 0.067 | 1.18E+07 | 0.105 | 1.44E+06 | 0.143 | 288745.2 |
| 0.068 | 3.47E+06 | 0.106 | 1.40E+06 | 0.144 | 259573.1 |
| 0.069 | 5.58E+06 | 0.107 | 1.36E+06 | 0.145 | 230056.1 |
| 0.07 | 2.91E+06 | 0.108 | 1.33E+06 | 0.146 | 200992.9 |
| 0.071 | 2.86E+06 | 0.109 | 1.29E+06 | 0.147 | 172842.6 |
| 0.072 | 2.82E+06 | 0.110 | 1.26E+06 | 0.148 | 114092.8 |
| 0.073 | 2.78E+06 | 0.111 | 1.23E+06 | 0.149 | 56366 |
| 0.074 | 2.74E+06 | 0.112 | 1.19E+06 | | |
| 0.075 | 2.69E+06 | 0.113 | 1.16E+06 | | |
| 0.076 | 2.65E+06 | 0.114 | 1.13E+06 | | |
| 0.077 | 2.60E+06 | 0.115 | 1.10E+06 | | |
| 0.078 | 2.56E+06 | 0.116 | 1.07E+06 | | |
| 0.079 | 2.51E+06 | 0.117 | 1.03E+06 | | |
| 0.08 | 2.47E+06 | 0.118 | 1.00E+06 | | |
| 0.081 | 2.42E+06 | 0.119 | 971938.2 | | |
| 0.082 | 2.38E+06 | 0.120 | 942220.1 | | |
| 0.083 | 2.33E+06 | 0.121 | 911346.2 | | |
| 0.084 | 2.29E+06 | 0.122 | 881899.9 | | |
| 0.085 | 2.24E+06 | 0.123 | 853012.6 | | |
| 0.086 | 2.20E+06 | 0.124 | 823145.4 | | |
| 0.087 | 2.16E+06 | 0.125 | 794342.2 | | |

## Visual Editor

Visual Editor® was used to ensure the accurate configuration of the room's geometry, human phantom positioning, and phantom characteristics. The software allowed for visualization and verification of the absence of surface overlaps and gaps, and it facilitated the thorough examination of the geometry from multiple angles, which enhanced the precision of the MCNP® model.

## MCNP® Benchmarking

The geometry of the model was confirmed using Visual Editor®. The input was then benchmarked by setting up a simulated room filled with air. A Cesium-137 emitter was positioned at the center of the room and the dose per emission was calculated. Using the F5 tally, dose coefficient conversion from ICRP 116 Table A.1 – AP value and assigning it to a detector cell positioned at 1 meter distance, the calculated outcome was $2.99 \times 10^{-5}$ pSv per emitted particle. This value is close to theoretical value of $2.87 \times 10^{-5}$ pSv per emitted particle (Parker,2022). The calculation of the effective doses at 1 meter and 0.5 meter utilizing F5 tallies in MCNP and ICRP 116 Table A.1 is shown in the Table 12.

Table 14: Effective dose calculation at 1 meter and 0.5 meter utilizing F5 tallies in MCNP and ICRP 116 Table A.1.

| **Energy bins** | **Effective dose per fluence (AP)** | **F-5 tally output fluence Φ at 1m** | **Dose per emission** | **F-5 tally output fluence Φ at 0.5 m** | **Dose per emission** |
|---|---|---|---|---|---|
| MeV | pSv $cm^2$ | $\frac{\text{photons}}{cm^{-2}}$ | $\frac{\text{pSV}}{\text{emission}}$ | $\frac{\text{photons}}{cm^{-2}}$ | $\frac{\text{pSV}}{\text{emission}}$ |
| 0.01 | 0.0685 | 1.657E-10 | 1.135E-11 | 1.44E-09 | 9.89E-11 |
| 0.015 | 0.156 | 1.718E-10 | 2.679E-11 | 9.71E-11 | 1.51E-11 |
| 0.02 | 0.225 | 1.718E-10 | 3.864E-11 | 9.71E-11 | 2.18E-11 |
| 0.03 | 0.313 | 6.821E-10 | 2.135E-10 | 7.14E-09 | 2.24E-09 |
| 0.04 | 0.351 | 6.101E-09 | 2.141E-09 | 1.00E-07 | 3.52E-08 |
| 0.05 | 0.37 | 1.432E-08 | 5.298E-09 | 2.40E-07 | 8.90E-08 |
| 0.06 | 0.39 | 1.693E-08 | 6.602E-09 | 3.02E-07 | 1.18E-07 |
| 0.07 | 0.413 | 1.836E-08 | 7.581E-09 | 3.34E-07 | 1.38E-07 |
| 0.08 | 0.444 | 1.845E-08 | 8.194E-09 | 3.62E-07 | 1.61E-07 |
| 0.1 | 0.519 | 3.284E-08 | 1.704E-08 | 6.41E-07 | 3.33E-07 |
| 0.15 | 0.748 | 5.99E-08 | 4.481E-08 | 1.25E-06 | 9.38E-07 |
| 0.2 | 1 | 2.054E-07 | 2.054E-07 | 2.61E-06 | 2.61E-06 |
| 0.3 | 1.51 | 5.416E-08 | 8.178E-08 | 1.79E-06 | 2.70E-06 |
| 0.4 | 2 | 1.745E-08 | 3.491E-08 | 3.11E-08 | 6.23E-08 |
| 0.5 | 2.47 | 1.431E-08 | 3.535E-08 | 2.69E-08 | 6.65E-08 |
| 0.511 | 2.52 | 1.111E-09 | 2.8E-09 | 1.31E-09 | 3.31E-09 |
| 0.6 | 2.91 | 1.059E-08 | 3.082E-08 | 7.41E-08 | 2.16E-07 |
| 0.8 | 3.73 | 7.894E-06 | 2.945E-05 | 3.17E-05 | 1.18E-04 |
| | | | 2.993E-05 | | 1.26E-04 |

*AP, antero-posterior

The dose per emission was calculated by multiplying the values from ICRP 116 Table A.1, Antero-posterior, with the corresponding F5 tallies output from the MCNP input decks, as shown in Appendix A.

Another MCNP input was written to calculate the dose at various locations inside the Radiology room. Locations of detector, direction of beam, equine phantom, and human phantom are shown in Fig 15.

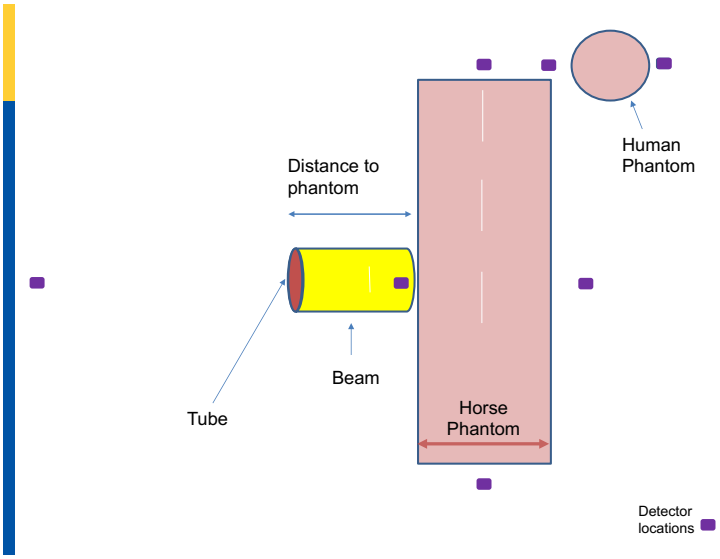

Figure 15: Radiology room showing detector location

Cell cards were used to define the material, density, boundary surfaces, and interactions inside the simulated radiology room. To simplify the MCNP® code and to reflect that no X-ray interaction occurred outside the walls of radiology, the area outside the walls was designated as vacuum. This model reflects a close approximation to radiology conditions as there were no surfaces to reflect the X-ray or external source of photons. The room was filled with air, and neutron interactions ignored. Surface cards were defined using macro bodies, a geometric feature for defining complex objects. Macro bodies were used to specify the rectangular parallelepiped (RPP) room dimensions in cm. Similarly, the Right Circular Cylindrical (RCC) defined the shape, dimension, and location of the horse and human phantoms.

Source cards were used to define the properties of the X-ray beam. A source definition card (SDEF) was used to specify the X-ray anode's position, shape, emission properties, dimension, and the beam's direction, shape, and energy distribution. The emitted photons were specified as an

energy distribution histogram, with SI values tabulated in 10 keV bins, and SP values normalized to 0-1. The SI and SP values were calculated using the SpekCalc® output shown in **Table 15**. The second set of SI and SP values defined a circular plane source. Then, another set of dE, dF, and *FM* cards was used to define the F5 tally. The *dE* and *dF* tallies were adopted from Table A1 of ICRP 116, where *dE* represents energy measured in keV and dF represents photon effective dose per fluence in pSv $cm^2$. A tally multiplier was used to convert the output to mSv. Materials property cards defined water and air. MCNP iterations were set to 10 billion.

Table 15: Photons in 10 keV energy bins for input 145 kVp

| Energy bins keV | Average energy keV | Number of photons | Normalized |
|---|---|---|---|
| 0-50 | 45 | 4376738 | 0.02 |
| 51-60 | 55 | 78920628 | 0.33 |
| 61-70 | 65 | 46321347 | 0.20 |
| 71-80 | 75 | 26685157 | 0.11 |
| 81-90 | 85 | 22224474 | 0.09 |
| 91-100 | 95 | 17989462 | 0.08 |
| 101-110 | 105 | 14192313 | 0.06 |
| 111-120 | 115 | 10824016.3 | 0.05 |
| 121-130 | 125 | 7808931 | 0.03 |
| 131-140 | 135 | 5006553.1 | 0.02 |
| 140-150 | 145 | 1990770.2 | 0.01 |
| | Sum | 236340389.6 | 1 |

A simulated dose for the most common setting of Thoracic Lumber was found to be 0.14 mGy where the measured dose was 0.14 mGy. Similarly, the highest setting was found to be 5.49 mGy while the measured dose was 4.10 mGy. Details are shown in **Table 15**.

Table 15: Dose summary for most frequent and highest setting

| kVp | mAs | Single Phase X-ray (mGy) | Multi-phase X-ray (mGy) | 451 P Measured (mGy) | R/F Measured (mGy) | | error (mGy) | Human Equivalent |
|---|---|---|---|---|---|---|---|---|
| 90 | 6 | 0.14 | 0.28 | 0.14 | 1.37 | ± | 0.04 | Thoracic |
| 145 | 100 | 6.03 | 12.06 | 4.10 | 13.07 | ± | 1.23 | CT scan |

The simulated doses were assessed at the following seven locations and are reported in **Table 16**: i.) the proximal side of the horse phantom to the X-ray tube; ii.) the distal side of the horse phantom to the X-ray tube, iii) the head of the horse phantom; iv) tail of horse phantom; v) chest height of human phantom located next to horsetail; vi) the back of human phantom; vii) and directly behind the X-ray tube.

Table 16: Simulated dose at various spatial locations

| | **Most frequent TF setting** | **Highest setting** |
|---|---|---|
| | (90 kVp &6 mAs) | (145 kVp, 0.2s, & 500 mA) |
| Detector locations | Units (µGy) | Units (µGy) |
| Tail of horse | 2.73E-03 | 1.07E-01 |
| Proximal side of the horse phantom | 1.40E+02 | 5.49E+03 |
| Distal side of the horse phantom | 2.82E-04 | 1.11E-02 |
| Chest height of human phantom located next to horsetail | 1.85E-03 | 7.25E-02 |
| Back of human phantom | 7.59E-05 | 2.98E-03 |
| Directly behind the X-ray tube | 3.02E-01 | 1.18E+01 |

Simulations indicate that the horse phantom absorbs a significant dose of radiation when focused at the center of the body. The dose behind the horse phantom is five to six orders of magnitude lower than the dose in front of it. The spatial location and angle relative to the beam determine the radiation dose received. Individuals directly in the primary beam are more likely to receive a higher radiation dose than those at 90 degrees to the beam. The data may be biased because multiple dose

assessments were not taken near or next to the tube, at various angles to reflect an accurate picture. The total dose received directly behind the emitter would be further lowered by interaction with the X-ray tube, collimator, and filter assembly.

## CONCLUSIONS

X-ray radiation is used daily at the Johnson Family Equine Hospital, and radiation workers and students are exposed to primary and scattered X-rays inside the radiology facility. It is essential to assess and track exposure to comply with regulations.

One way to assess X-ray exposure is to characterize the transmission and scattering of X-rays. This study shows tracking can be done using a direct measurement instrument, but it has limited feasibility due to its limitations of instruments and potential unnecessary exposure to X-rays. Instead, a Monte Carlo simulation can be used to understand transmission and scattering. A Software like SpekCalc® can be used to generate a spectrum for each technique factor used in the radiology room. Then, a Monte Carlo simulation replicated the conditions inside the radiology building, including equine and human phantoms, X-ray beam characteristics and direction, room geometry, and interaction between phantoms and beams.

The simulation facilitated the quantification of effective doses across various spatial points. The simulated absorbed dose was highest in the primary beam, and lowest at a 90-degree angle from the direction of the beam, at the same distance from the source. The absorbed dose also differed considerably in front of and behind the phantoms due to photoelectric absorption. This information can be used to develop strategies to reduce X-ray exposure for radiation

workers and students. For example, workers' or students' elevated exposure could have resulted from exposure to the primary beam. Thus, it is recommended that they should position themselves outside the primary beam whenever possible. Radiation workers should also continue to wear appropriate personal protective equipment, such as lead aprons and gloves. By assessing the transmission and scattering of X-rays, the Johnson Family Equine Hospital can help to ensure the safety of its radiation workers and students.

## REFERENCES


Anderson, C. D. (1932). The Positive Electron. Physical Review, 43(7), 491-494.

American Association of Equine Practitioners. (n.d.). Radiography. Retrieved from https://www.aaep.org/horse-owners/radiography

Bassler, N. (2011). Photoelectric effect and X-ray imaging. Radiology, 259(2), 264-271.

Clark, R. J. H., & Roberts, A. W. (1957). Photodisintegration of Deuterium. Nature, 180(4588), 555-556.

Characterization of X-ray sources used in industrial radiography. Journal of Applied Radiation and Isotopes, Vol. 70, Issue 8, August 2012, Pages 2104-2109

Choppin, G. R. (2014). Radiochemistry and Nuclear Chemistry. Butterworth-Heinemann.

Compton, A. H. (1923). A Quantum Theory of the Scattering of X-rays by Light Elements. Physical Review, 21(5), 483-502.

Einstein, A. (1905a). Über einen die Erzeugung und Verwandlung des Lichtes betreffenden heuristischen Gesichtspunkt. Annalen der Physik, 17(6), 132–148.

Hall, E. J., & Cunningham, J. R. (1991). Radiation protection in medical radiography. Physics in Medicine and Biology, 36(1), 1–17.

International Commission on Radiological Protection (ICRP). (2007). The 2007 Recommendations of the International Commission on Radiological Protection. ICRP Publication 103.

International Commission of Radiological Protection (2010). The 2010 Conversion Coefficients for Radiological Protection Quantities for External Radiation Exposures. ICRP Publication 116

International Commission on Radiation Units and Measurements (ICRU). (1998). Conversion Coefficients for Radiological Protection Quantities for External Radiation Exposures. ICRU Report 57

Johnson, T. E. (2017). Introduction to Health Physics (5th ed.). McGraw-Hill.

Knoll, G. F. (2010). Radiation Detection and Measurement (4th ed.). Hoboken, NJ: Wiley.

Lambrecht, J. (2017). Imaging of the equine hip. Equine veterinary education, 29(9), 472-478.

Los Alamos National Laboratory (2008). MCNP® ® User Manual, Version 5. Los Alamos, NM; LANL.

NCRP Report No. 160, Ionizing Radiation Exposure of the Population of the United States. Bethesda, MD: National Council on Radiation Protection and Measurements; 2009.

NCRP Report No. 147. National Council on Radiation Protection and Measurements. Structural shielding design for medical X-ray imaging facilities. 2004.

Optimization of X-ray energy spectra for medical imaging. Physics in Medicine and Biology, Vol. 61, Issue 8, April 2016, Pages 2900-2918

Rayleigh, J. W. S. (1871). The scattering of light by a transparent sphere. Philosophical Magazine Series, 42(249), 81–106.

Röntgen, W. (1895). On a new kind of rays. Sitzungsberichte der Physikalisch Medizinischen Sozietät zu Würzburg, 22(3), 132-148.

"Report 57," in Journal of the ICRU, vol. os29, no. 2, pp. NP-NP, Aug. 1998, doi: 10.1093/jicru/os29.2.Report57.

S. A. A. -. (2010). Characterization of the R/F Ionization Chamber for Clinical Dosimetry. Journal of Applied Clinical Medical Physics, 11(4), 4234-4241.

Sarofim, A. F., & Hanson, R. K. (1988). X-ray attenuation coefficients. Physics in Medicine and Biology, 33(9), 1069.

## APPENDIX A

Dose conversion table modified from ICRP 116. Photons: effective dose per fluence, in units of pSv $cm^2$, for mono- energetic particles incident in various geometries.

| Energy bins | Antero-Postero |
|---|---|
| (MeV) | (pSv $cm^{-2}$) |
| 0.01 | 0.0685 |
| 0.015 | 0.156 |
| 0.02 | 0.225 |
| 0.03 | 0.313 |
| 0.04 | 0.351 |
| 0.05 | 0.37 |
| 0.06 | 0.39 |
| 0.07 | 0.413 |
| 0.08 | 0.444 |
| 0.1 | 0.519 |
| 0.15 | 0.748 |
| 0.2 | 1 |
| 0.3 | 1.51 |
| 0.4 | 2 |
| 0.5 | 2.47 |
| 0.511 | 2.52 |
| 0.6 | 2.91 |
| 0.8 | 3.73 |